DISPERSE

Electronics for spatially distributed sensors and transducers arrays

Labeled in PENTA, a EUREKA cluster, Call 1

PENTA Project Number 16012

D4.1 – Proof of Concept for Scanning Multiple Implants

Due date of deliverable: M30

Start date of project: 1 February 2017	**Duration:** 36 months
Organisation name of lead contractor for this deliverable:	Cochlear
Author(s):	Philip Joris (KU Leuven), Guy Fierens (Cochlear), Edoardo Paoles (GTX medical)
Status:	Final
Version number:	2.0
Date:	January 24, 2020
Doc reference:	DISPERSE_Deliverable_D4.1_POC_Scanning_Multiple_Implants_V1.3.docx
Work Pack./ Task:	WP4 T4.1
Description: ***(max 5 lines)***	This document describes development and experiments conducted to prove the feasibility of scanning multiple implants.

Nature:	<Use one of these codes: **R**=Report, **P**=Prototype, **D**=Demonstrator, **O**=Other>		
Dissemination Level:	**PU**	Public	**X**
	PP	Restricted to other programme participants	
	RE	Restricted to a group specified by the consortium	
	CO	Confidential, only for members of the consortium	

DOCUMENT HISTORY

Release	Date	Reason of change	Status	Distribution
V0.1	08/10/2019	First draft with template tables	Draft	KU Leuven, GTX medical, Cochlear
V0.2	20/10/2019	Added sections 4.1, 4.2, and 4.4.	Draft	KU Leuven
V0.3	04/11/2019	Added Cochlear input	Draft	KU Leuven, GTX medical, Cochlear
V0.4	06/11/2019	Added GTX input	Draft	KU Leuven, GTX medical, Cochlear
V1.0	07/11/2019	Finalised v1.0 of document.		All partners
V1.1	27/12/2019	Added results from multi-implant experiments.		All partners
V1.2	08/01/2020	Small changes to text.		All partners.
V1.3	23/01/2020	Small changes to text.	Final	All partners.
V2.02	24/01/2020	Submitted to portal	Final	PENTA Office

Table of Contents

Glossary

Abbreviation / acronym	Description
AIMD	Active Implantable Medical Device
SCS	Spinal Cord Stimulator
FE	Frequency Encoding
GTX	GTX medical
ICM	Iterated Conditional Modes
IPG	Implantable Pulse Generator
MAVRIC	Multi-Acquisition Variable Resonance Image Combination
MEI	Middle-Ear Implant
MI	Mutual Information
MRF	Markov Random Field
MRI	Magnetic Resonance Imaging
PE	Phase Encoding
SCI	Spinal Cord Injury
SEMAC	Slice-Encoding for Metal Artefact Correction
SNR	Signal to Noise Ratio
TESS	Targeted Epidural Spinal Stimulation

1 Executive Summary

This document discusses the integration of technological developments into active implantable medical devices, the development of ex-vivo setups for testing single- and multi-implant scanning, and the effects of acquisition parameters and post-processing methods on image quality as per deliverable 4.1.

2 Introduction

Because of population aging, it is estimated that by 2020 7.2% of the general population and 28% of the 65+ people will have 1 or more implants. State-of-the-art MR conditional implant testing only takes into account the individual implant under test in the environment of an MR scanner. Within DISPERSE, we therefore investigated various, realistic constellations of middle-ear implants (MEIs) and a spinal cord stimulator (SCS).

The patient hazards involved with scanning active implantable medical devices (AIMDs) are thoroughly described in ISO/TS 10974 [1]. For a spinal cord stimulator, RF heating of the lead is considered to be the most critical interaction, since this might lead to tissue damage at extremely sensitive anatomical sites (e.g. spinal cord). In the case of hearing implants, on the other hand, the main concern are large image distortions that make the evaluation of brain scans unfeasible. This document describes experiments that were conducted within DISPERSE to assess these effects using ex-vivo setups.

Section 3 first focuses on the integration of developed technologies into a spinal cord stimulator and a fully implantable middle ear implant. Next, section 4 describes the experimental setups that were used to evaluate various AIMD constellations. This includes the development of ex-vivo setups, the acquisition parameters, and the evaluation of RF-heating and imaging artefacts. In section 5 then, we describe a post-processing method to reduce the size of resulting imaging artefacts using multiple acquisitions from a single patient. Section 6, finally, presents the main conclusions.

3 Integration of Components

The focus in WP4 is on the integration of components that were developed in WP2 and WP3 into complete AIMDs. In this section, we discuss the development of a SCS developed by GTX medical and the Carina® MEI developed by Cochlear respectively.

3.1 Spinal Cord Stimulator

Based upon the research from Prof. Grégoire Courtine from the Ecole Polytechnique Fédérale de Lausanne (EPFL), G-Therapeutics (GTX) is developing the Go-2 Targeted Epidural Spinal Stimulation (TESS) therapy to make people with spinal cord injury (SCI) walk again. The TESS therapy combines an implantable neuro-stimulation system with real-time motion feedback with an intensive rehabilitation program (e.g. using body weight-assisted training tools). More specifically, the Go-2 system consists of an implantable pulse generator (IPG), 16-electrode paddle lead, motion sensors, and motion controller, as seen on the left of Figure 1.

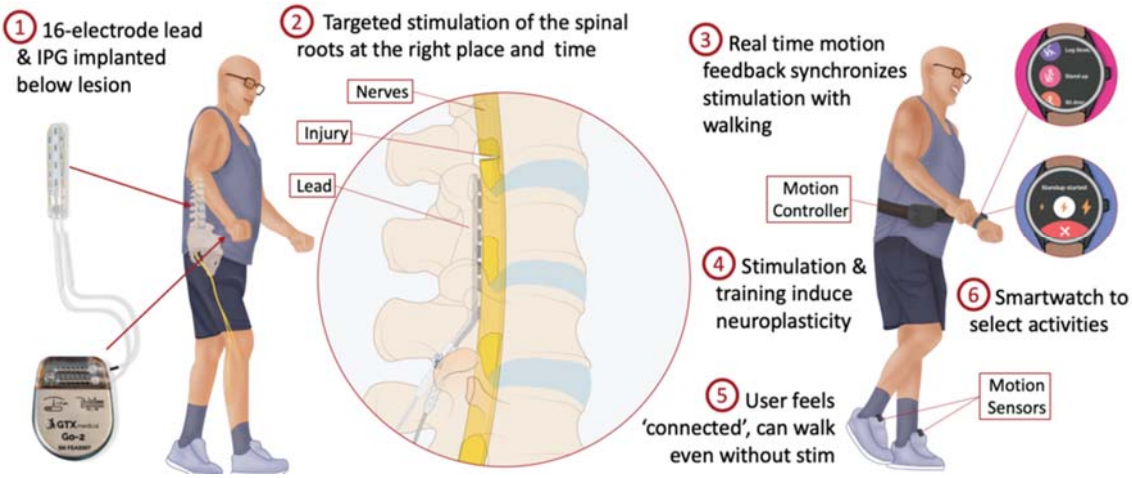

Figure 1: GTX TESS therapy

GTX considers MRI safety a crucial feature of the Go-2 system. Therefore, GTX has integrated the relevant findings from the DISPERSE project in the electronics development of the implantable pulse generator and paddle lead and is currently working towards the MRI Conditional label.

3.2 Active Hearing Implant

The Cochlear™ Carina® implant is a fully implantable MEI for patients with moderate to severe sensorineural, conductive or mixed hearing loss. The Carina MEI features a sensitive implantable microphone to pick up sound which is amplified in the implant body and converted into mechanical vibrations by the implantable actuator to stimulate a patient. Depending on a patient's specific needs, the actuator can be coupled to the ossicles, the oval window or the round window to compensate for the hearing loss.

In normal operation, the Carina system works as follows (see Figure 2):

1. The implantable microphone (1) captures sound through the skin and sends it to the implant body (2) for processing.
2. The implant body processes the sound and generates and electrical signal.

3. The signal gets transferred to the T2 middle ear actuator (3) coupled to the patient's middle ear structures (4).

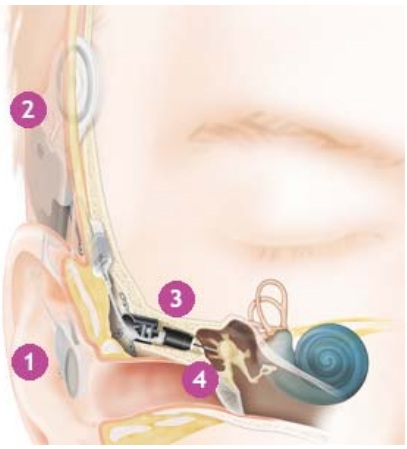

Figure 2: Schematic overview of the Carina system

The implant body also features an implanted coil and a retention magnet (see Figure 3) for coupling the implant with the battery charger and with external accessories like the button audio processor to improve hearing in noisy environments.

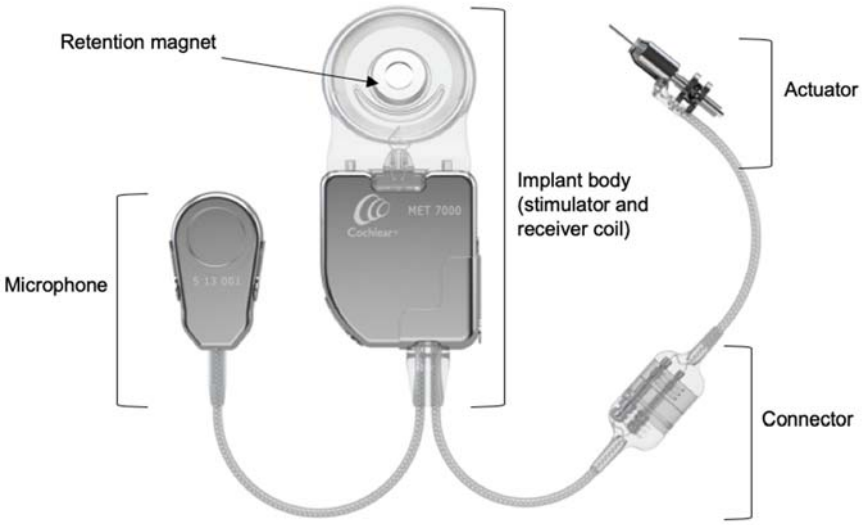

Figure 3: Carina implant

Currently, the Carina implant is labelled MRI unsafe. During the DISPERSE project, multiple technological innovations have been defined that could improve the MRI safety of these fully implantable devices, mainly focussing on the middle ear transducer and transcutaneous implantable microphone components. Further internal research and characterization work is ongoing to mature these novel technologies.

4 Multi-Implant Co-Existence

4.1 Ex-Vivo Phantoms

To evaluate the effects of (co-existence of) implants in an MR scanner, we tested several realistic constellations. To this end, we first developed several phantoms. Figure 4, Figure 5, and Figure 6 show one geometric and two human head phantoms. The first phantom (Figure 4) consists of a simple rectangular grid and plastic container to hold implants. The fixed dimensions and regular geometry enable us to accurately assess the effects of implants and their materials on image quality. The phantoms from Figure 5 and Figure 6, on the other hand, resemble a human head [3]. In Figure 5, a plastic tube is used to represent the spine, whereas a more realistic spine (and mandible) are present in the phantom from Figure 6. As can be seen, both phantoms allow for a more anatomically correct positioning of MEIs.

Before scanning, each of these phantoms is placed in a container that is filled with a paramagnetic liquid to simulate tissue properties and increase image contrast. In our experiments, we used a mixture of tap water and copper sulphate, mixed with a ratio of *2g/l* as prescribed in ASTM F2119 [2] (with the exception of the heating experiments described in section 4.2).

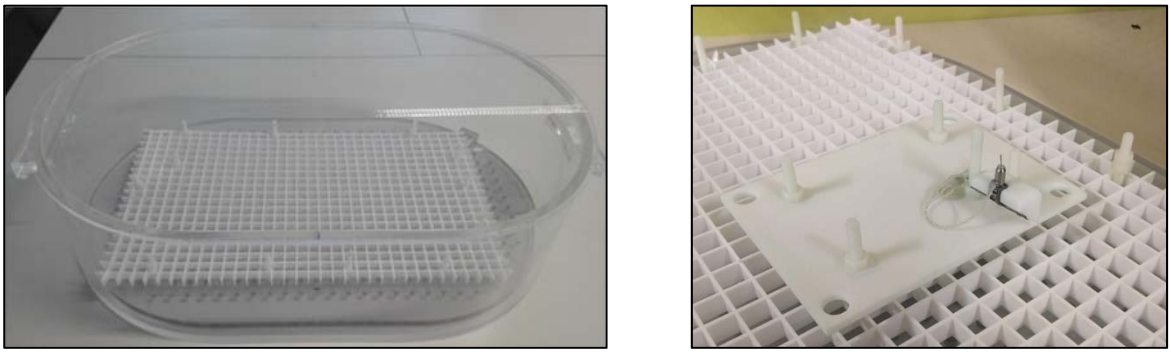

Figure 4: GTX phantom consisting of a container, regular grid, and plastic casing with middle ear implant.

Figure 5: Human head phantom with simple spine and middle ear implant.

Figure 6: Human head phantom with realistic spine, mandible, and middle ear implant.

4.2 RF-Heating

As stated in ISO/TS 10974 [1], RF-heating is a primary patient hazard for neurostimulators. Simulations regarding heating were performed and described in the public deliverable 2.4 [4]. To confirm these simulations, we performed an ex-vivo experiment using the phantom from Figure 4. Within this phantom, implant(s) were mounted in a similar way as they were modelled[1]. Based on the simulation results described in the DISPERSE deliverable D2.4, temperature sensors (THR-NS-1165F, FISO Technologies Inc, Quebec, Canada) are mounted in close proximity to the calculated hotspots. A minimum positioning accuracy of 0.25 mm with respect to the implant hotspot is maintained as prescribed in clause 8 of ISO/TS 10974 [1] for SAR-based simulations. In addition, an additional temperature sensor is mounted at least 10 cm away from the implant(s) to measure background heating.

Once all components were mounted, the phantom was put on the patient bed inside the MRI suite and filled with a tissue simulating medium. This medium (or gel) was prepared as described in annex L of ISO/TS 10974 (2018) [1]. The gel material is made in a separate container before the start of the experiment and consists of a mixture of 96.85 % water, 3% Hydroxyethyl Cellulose (HEC) and 0.15% NaCl, resulting in a relative dielectric permittivity of 78 and a conductivity of 0.47 S/m which is a high permittivity medium (simulating the immediate surroundings of the implant) with an electrical conductivity simulating the global average of biological tissues). Finally, the phantom was moved forward into the patient bore for scanning in the different simulated positions [4]. The complete setup is shown in Figure 7 below.

A turbo spin echo sequence was defined with parameters similar to the pulse sequence parameters proposed in ASTM F2182 [5]. A summary of the sequence parameters can be found in Table 1. In total, three different configurations are tested:

1. Multi-implant coexistence when a spinal cord stimulator electrode is in close proximity (~70 mm) to the Carina middle ear actuator.
2. Single-implant configuration where only the spinal cord stimulator is placed in the phantom, in the same position with respect to test case 1.
3. Single-implant configuration where only the middle ear implant is placed in the phantom, in the same position with respect to test case 1.

The heating of the gel surrounding the implants is measured in each test case when the phantom is located in the isocentre, placing the middle of the electrode pad, middle ear actuator, middle ear implant and IPG on an axis intersecting the isocentre. Afterwards the phantom is moved 15 cm out of the isocentre before repeating the measurement.

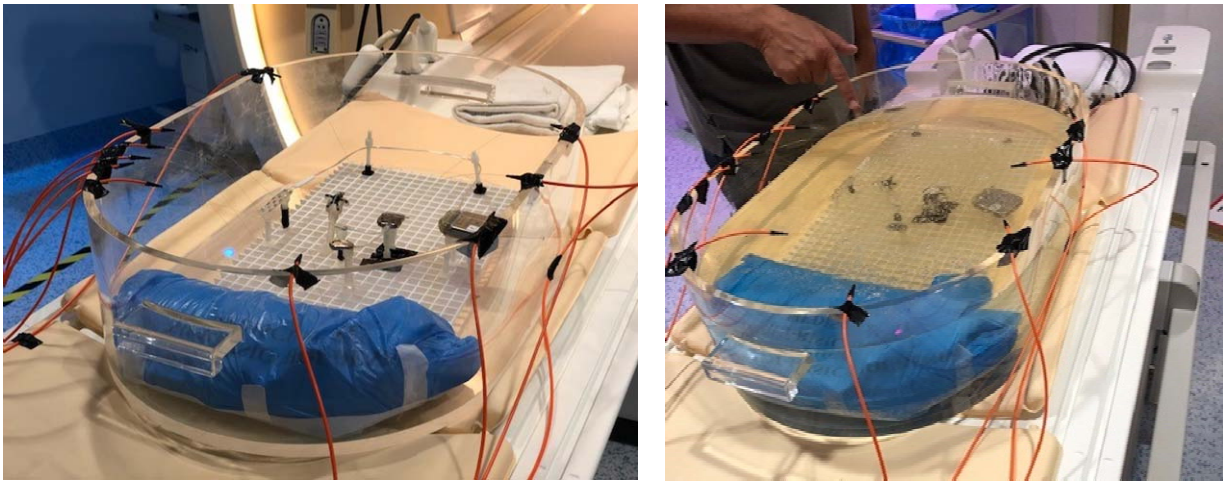

Figure 7: Implants are mounted inside the phantom to mimic the simulated test cases [4] before (left) and after filling the phantom with gel (right).

[1] For more information regarding the computer models, the reader is referred to public deliverable 2.4 [4].

Table 1: Scan parameters

MRI Parameter	ASTM F2182 value	Value used
Sequence	Turbo spin echo	Turbo spin echo
TR	260 ms	169 ms
TE	6 ms	6 ms
Echo train length	16	16
Plane	Coronal	Coronal
Flip angle	90°	90°
Bandwidth	69 kHz	1007.4 Hz/px
Field of view	45 cm	45 cm
Matrix	264 x 256	264 x 241
Section thickness	10 mm	10 mm
Total slices	4	4
WBA-SAR	4 W/kg	< 2W/kg
NSA	27	27
Dynamics	4	6
Scan time	15 min 11 sec	24 min 39 sec

Results of the experiments indicate that the coexistence of multiple implants in close proximity to each other affects the amount of heating at the predefined hotspots. Increased heating was observed in both implants, both in the single- and multi-implant cases when the phantom was moved outside of the isocentre. The maximum amount of heating during the experiments was observed at the contact area between the spinal cord stimulator electrode pads and the gel. The temperature increase after 25 minutes of scanning was approximately 20% higher when the spinal cord was mounted in the phantom together with the middle ear implant. Temperatures measured at the hotspots defined for the middle ear implant remained low during the entire experiment, indicating no significant heating around this device. Both in a single-implant and multi-implant configuration the observed temperatures were similar to temperatures observed by reference sensors. This could, at least in part, be due to the location of this device in the phantom. As the middle ear implant is mounted in the centre of the implant, it is exposed to electrical fields that are significantly smaller compared when it would be mounted more towards the side of the phantom.

4.3 Imaging Artefacts

In addition to the dangers of lead heating, AIMDs introduce magnetic susceptibility artefacts that drastically reduce diagnostic quality of an image. Even when implants are deemed MRI-safe, they can still impede the imaging process [6,7]. On the one hand, these artefacts are the result from local magnetic field

inhomogeneities introduced by magnetic objects into the otherwise homogeneous external magnetic field B_0. On the other hand, current induced by the gradient/RF fields in conductive structures of the AIMDs generate local magnetic fields that lead to distortions. Susceptibility artefacts are characterized by a loss of signal, dephasing, and spatial distortions, both in-plane and through-plane [9].

In this session, we assess if and how individual implants and constellations of multiple implants affect the size and shape of the resulting artefact. To this end, we first define several imaging sequences, as the effect of metallic implants on artefact size can be reduced through careful selection of the acquisition parameters (section 4.3.1). After that, we scan individual implants (sections 4.3.2 and 4.3.3) as well as multiple implants (sections 4.3.4 and 4.3.5) and evaluate the size of the resulting artefacts.

4.3.1 Acquisition Parameters

It is well known that a careful selection of acquisition parameters can drastically affect image quality in cases with metallic implants. In literature, the following general conclusion are made. First and foremost, signal loss (i.e. dark regions in the resulting MR images) are minimal when using spin echo techniques [6] (as opposed to gradient echo techniques) and shorter echo spacing [8]. This is clearly illustrated in Figure 8, showing scans from a MEI using fast field echo (middle) and spin echo (right). Distortions can further be reduced by maximizing bandwidth for both slice selection and slice readout [6]. Lowering field strength decreases artifacts as well.[8]. Moreover, we can reduce the effects of signal loss and signal pile-up by using view-angle tilting (VAT) [6,8,9]. Finally, we can reduce spatial distortions in the slice direction by using thinner slices [6,10] and smaller voxels [8], though this does increase scanning time while decreasing SNR as voxel sizes are reduced. In [10], the authors claim that increasing in-plane resolution results in the least benefit and should thus be looked at first to reduce scanning time. Also, SNR can of course be recovered somewhat by averaging multiple slices in a post-processing step [6,10].

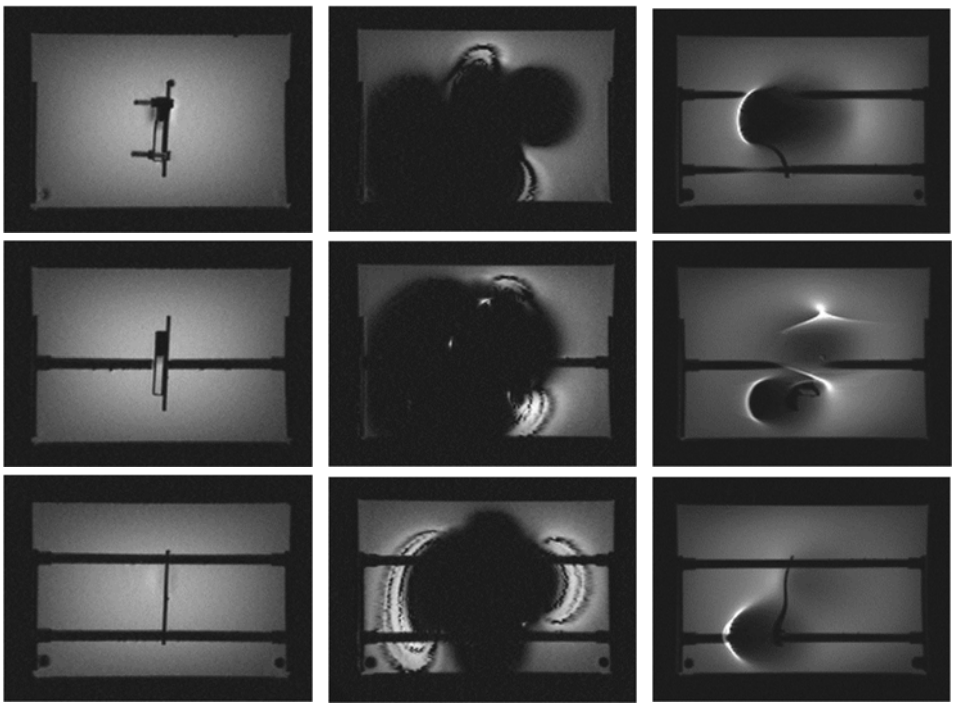

Figure 8: Phantom without MEI (left), and phantom with MEI by fast field echo (middle) and spin echo (right).

Using the above suggestions, one can define a custom imaging sequence to minimize the effect of metallic implants on the resulting image. Alternatively, one can rely on existing protocols that were specifically designed to image metallic implants. GE Healthcare, for example, developed the multi-acquisition variable resonance image combination sequence, or MAVRIC in short. MAVRIC combines acquisition techniques

and post-processing to image soft tissue and bone near metallic devices. Both in-plane and through-slice displacement artefacts [1] are corrected by relying on frequency-selective excitation (as opposed to slice excitation). This means that several images are acquired, which are then combined during post-processing. Another approach is Slice-Encoding for Metal Artefact Correction (SEMAC), again correcting both in-plane and through-slice distortions near metallic implants. SEMAC acquires 3D volumes of individual slices, using VAT to avoid in-plane artefacts. Multiple images of varying spatial bands are then combined to create the complete image.

In Figure 9, a comparison of three acquisition sequences is shown. From left to right, a MEI is shown that was scanned using an optimised spin echo (henceforth referred to as 'CUSTOM'), a standard MARS, and a SEMAC sequence. The CUSTOM sequence uses limited read-out bandwidth, small voxel size, and VAT. Note that distortions are the most severe in this image, although it is the sharpest outside affected regions. MARS uses VAT, slightly reducing distortions, but also increasing blurriness. SEMAC, finally, contains the least amount of distortions, but is also the blurriest. This is because SEMAC combines various images of varying spatial bands.

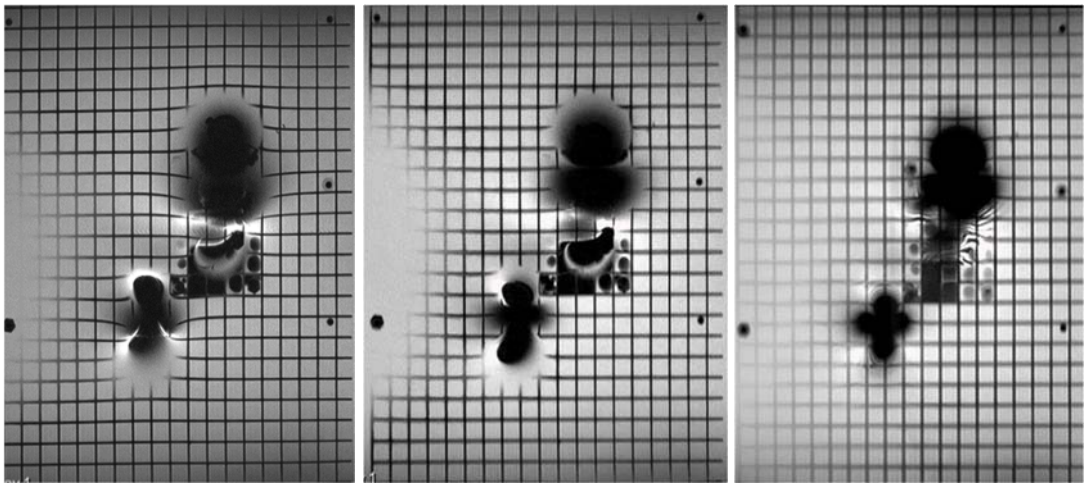

Figure 9: Comparison of CUSTOM acquisition (left), MARS sequence (middle), and SEMAC acquisition (right).

In the next few sections, we discuss two single- and two multi-implant setups that were scanned using the aforementioned CUSTOM sequence. In each section, we present images and measurements to illustrate the effect of the AIMDs on the size and shape of the resulting image artefacts. Each measurement was made on the slice with the largest artefact. The CUSTOM sequence was selected for two reasons. First, this sequence is based on some simple rules of thumb (see section 4.3.1), meaning that it can be created on any type of scanner. And second, the CUSTOM sequence produced the largest image artefacts, creating a worst-case scenario.

4.3.2 Spinal Cord Stimulator

The GTX Spinal Cord Stimulator (SCS) introduced in section 3.1 was attached to the skull-phantom shown in Figure 6, and scanned using the CUSTOM sequence. We then measured the diameter of the artefact around the lead and implant head. As seen in Figure 10, the artefact around the lead has a diameter of approximately 18mm to 40mm, which is rather small. In Figure 11, the artefact around the implant head is shown, which has a width of approximately 45mm. The length of the artefact around the head is approximately 105mm, which is mainly due to the physical size of the implant (around 7cm). Taking this size into account, the distortion roughly extends just 1.5cm on all sides of the implant head.

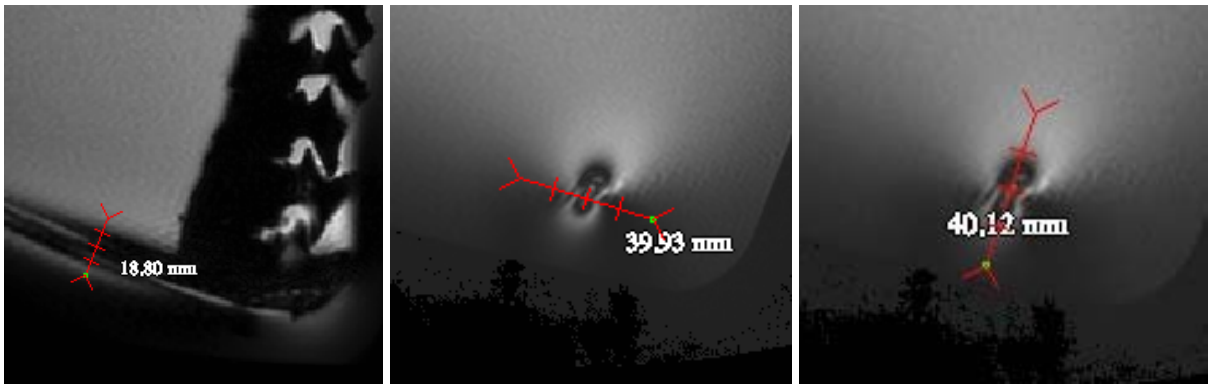

Figure 10: Distortion around lead of the SCS using CUSTOM sequence.

Figure 11: Distortion around SCS head using CUSTOM sequence.

4.3.3 Single Middle Ear Implant

In Figure 12, a single MEI is shown, scanned using our CUSTOM sequence and the phantom from Figure 5. We selected the slice with the largest in-slice artefact, having a length and width of approximately 160mm and 110mm respectively. Note that the artefact caused by the MEI is significantly larger than that caused by SCS. Of course, the MEI itself is larger than the SCS, but the large signal voids (black areas) are mostly

caused by the presence of magnetic materials (e.g. the retention magnet). These materials perturb the external magnetic field B_0, leading to the large signal voids (black areas) in Figure 12.

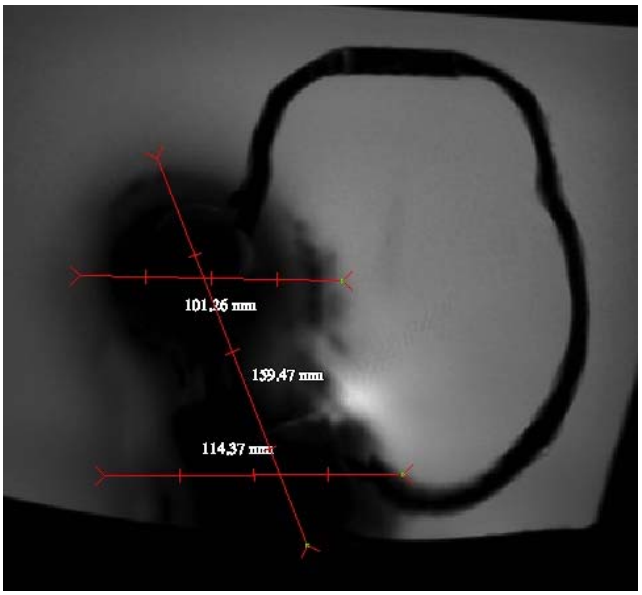

Figure 12: Maximum in-slice diameter of a single MEI scanned using the CUSTOM sequence.

4.3.4 Multiple Middle Ear Implants

To determine the influence of multiple implants, we positioned two MEIs bilaterally on the phantom shown in Figure 6. In Figure 13, several slices with measurements of the artefacts are shown. Two things are worth noting. First, comparing the artefacts with that from Figure 12, the shape is somewhat different. This is most likely due to the difference in implant positioning. Comparing Figure 5 and Figure 6, there is a clear difference in how the MEIs are positioned on the phantom as well as with respect to each other. This difference in positioning leads to a significantly different artefact shape. And second, it appears that the artefacts of the implants do not seem to interfere, as there is no overlap between the artefacts.

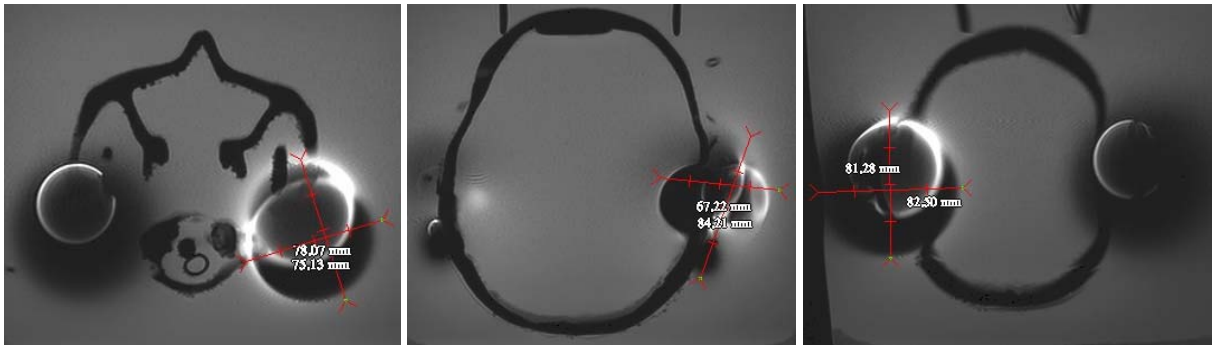

Figure 13: Two middle ear implants showing large distortions on the actuator (left), microphone (middle), and retention magnet (right) in the CUSTOM sequence.

4.3.5 Spinal Cord Stimulator and Multiple Middle Ear Implants

Finally, we repeated the experiment with two MEIs and added the SCS, taking care to position the MEIs as before and as symmetrical as possible. The slice with maximum artefact size is shown in Figure 14. Note how the artefact sizes are comparable to those in Figure 13, while being symmetrical as well. Again, note that the presence of the SCS did not seem to influence the size or shape of artefact of the MEIs and vice versa.

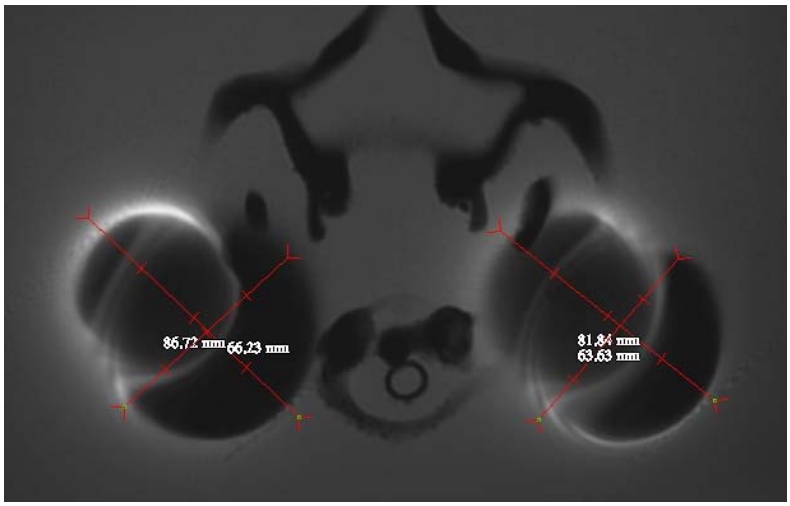

Figure 14: Two actuators of MEIs symmetrical in MARS sequence. No interference with SCS.

5 Image Post-Processing

Section 4.3 illustrated that the choice of imaging sequence clearly affects the size of the artefact as well as overall image quality. However, even with specialised acquisition protocols, reconstructed images still contain artefacts. In this section, we research if (and how) post-processing of reconstructed image(s) can further reduce the size of the artefacts. To date, and to the best of our knowledge, there are no post-processing methods in existence that reduce magnetic susceptibility artefacts in reconstructed images.

5.1 Multi-Acquisition Reconstruction

To reduce artefact sizes, we had a look at the frequency encoding (FE) and phase encoding (PE) directions. These directions can be set arbitrarily but are often set in specific ways to avoid certain artefacts. Wrap-around artefacts, for example, can be reduced by settings the phase-encoding direction along the shortest anatomic dimension. When imaging patients with metallic implants, however, there are no such general rules of thumb, and ad-hoc tuning is often required. By changing the PE and FE directions, resulting artefacts may change in appearance or move away from a region of interest (e.g. the brain). To test this, we used the head phantom from Figure 5 and a single MEI. The implant was attached to the phantom, and placed in a plastic container, which was again filled with a paramagnetic fluid (20 litres of tap water mixed with 40 grams of copper sulphate). The phantom was then imaged multiple times using the CUSTOM and SEMAC sequences, changing the PE and FE directions with 45° increments. Several slices from several acquisitions from the CUSTOM sequence are shown in Figure 15. Note how the signal loss remains the same whereas signal pileups indeed change in location and size.

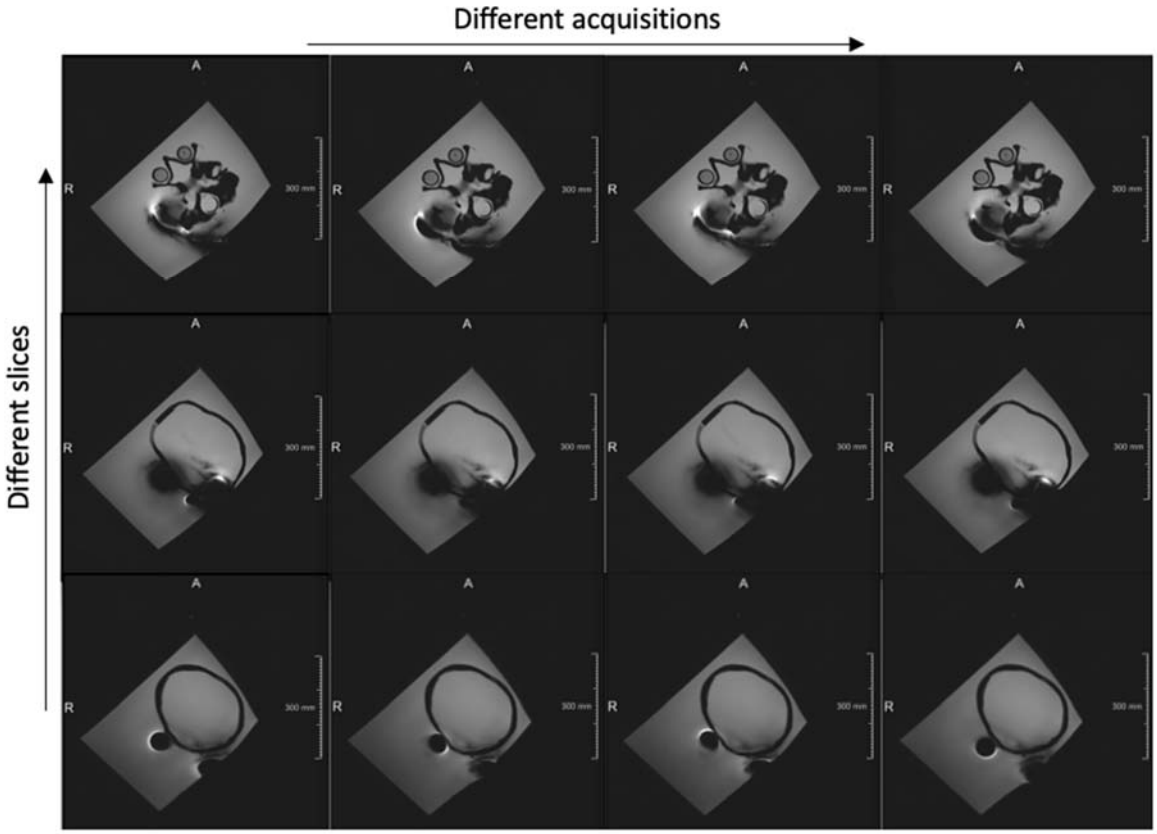

Figure 15: The same phantom imaged multiple times with varying encoding directions. Note how the size and appearance of the artefact changes slightly in between acquisition.

In theory, we can thus image the same patient multiple times using varying PE and FE directions and combine all images so that the overall size of the artefact is somewhat reduced. To test this, we created four different datasets, as summarised in Table 2. Each row represents a different dataset, and indicates how many implants were used, how many acquisitions were made (e.g. how many times the PE and FE directions were changed), what acquisition sequence was used, and what reference image is used. These reference images are simply the phantom without any implant, meaning that it will not contain any artefacts, which is used to evaluate the severity of an artefact.

Table 2: Datasets to evaluate the proposed post-processing technique.

Dataset name	Implants	# of Acquisitions	Sequence	Reference
DS1	1 MEI	8	CUSTOM	CUSTOM without implant
DS2	1 MEI	8	SEMAC	SEMAC without implant
DS3	2 MEI	6	CUSTOM	Standard T2 without implant
DS4	2 MEI	6	SEMAC	Standard T2 without implant

Once acquired, we combined all images such that the combined image contains an artefact of minimum size. In other words, the combined image contains artefacts in regions where *all* images from the dataset have an artefact. To create this combined image, the following five steps were taken:

1. First, all images (including the reference image for validation purposes) are spatially aligned and resampled so that they have corresponding voxel locations. Alignment of the images is done by using Elastix registration software [12]. Figure 16 shows the same slice from an arbitrary scan from DS1 and DS2 as well as their corresponding reference image.
2. The intensities of the images are then standardised using a simple percentile-based rescaling, whereby the histogram of each image was transformed using a piecewise linear transformation so that it matches a reference histogram. Though simple, this method suffices as we are standardising the intensities of images of the same patient and anatomical region. Figure 17 and Figure 18 show several image histograms before and after intensity standardisation respectively.
3. Next, we score each voxel in each image by comparing them to our template scan using absolute differences. Note that the template was registered affinely to the images with MEI to score voxels in our experiments. In practice, however, one would need to replace this template with an anatomical atlas and register the atlas non-rigidly to the patient images.
4. Based on the calculated scores, we create a recombined image using a maximum likelihood (ML) criterion. Each voxel in the combined image has the corresponding intensity of the image with the lowest score (e.g. the smallest intensity difference with respect to the template image).
5. The combined image removes part of the artefact. However, because the combined image is created voxel-wise, small discontinuities can arise. To increase smoothness of the combined image, and increase its perceptual quality, we apply a final smoothing step. To prevent blurring of edges, we use an approach that relies on a Markov random field (MRF) with robust L1-potentials. Image voxels are nodes whereas all possible intensities are labels for the MRF, giving rise to the following cost function:

$$\underset{x}{\operatorname{argmin}}\, \alpha \sum_{i}^{n} |x_i - y_i| + (1-\alpha) \sum_{(i,j)}^{m} |x_i - x_j|$$

Here, x contains the complete labelling of the smoothed image (e.g. its intensities), and x_i and y_i reference the intensity at voxel i in the smoothed and original image respectively. The summations run over all unary and pairwise cliques in the MRF, whereas α is a scaling factor that trades off smoothness to data trueness. Lower values for α will thus result in smoother result. The cost function is minimised using a simple Iterated Conditional Modes (ICM) optimisation process. In our experiments, α was set to 0.5.

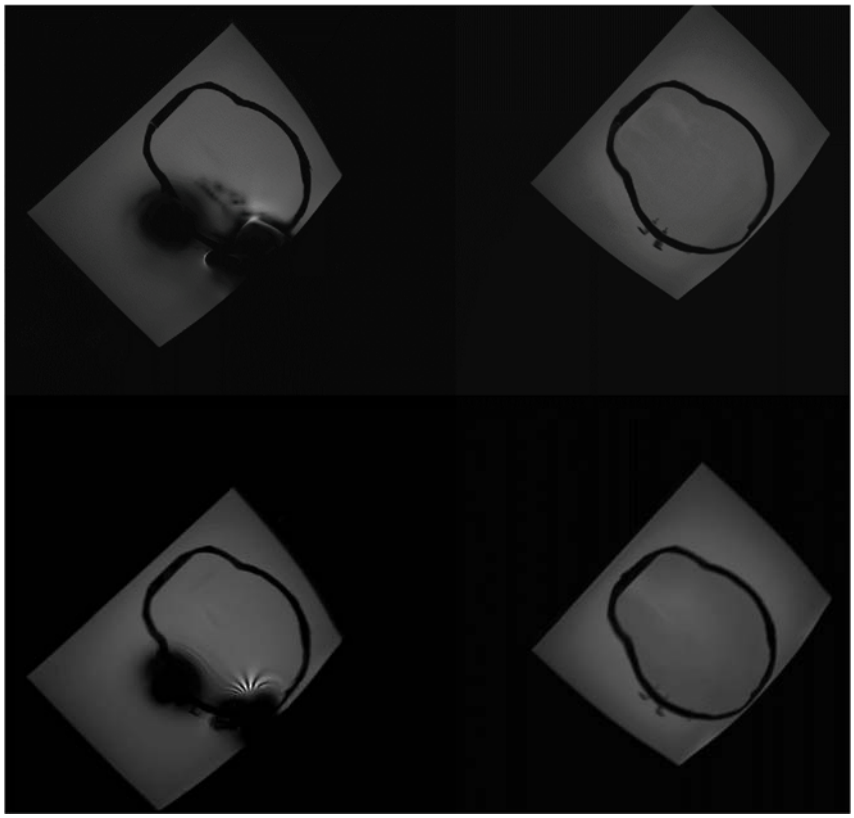

Figure 16: The same slice from the CUSTOM (top) and SEMAC (bottom) sequences of phantom with (left) and without (right) MEI.

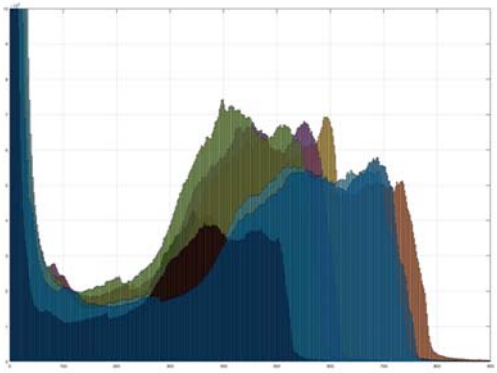

Figure 17: Histograms of SEMAC images before intensity standardisation.

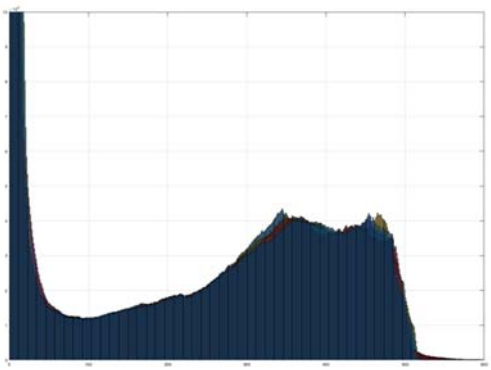

Figure 18: Histograms of SEMAC images after intensity standardisation.

5.2 Evaluation & Results

The approach described above reduces the size of the artefact by combining multiple acquisitions with varying PE and FE directions. Qualitatively, one can identify regions in the neighbourhood of the MEI in the combined image that are free of artefact whereas they are covered by the artefact in some original images. This is illustrated in Figure 19 and Figure 20, showing results from the CUSTOM and SEMAC sequences respectively. To quantify the improvement made by our method, we compare the original images, the ML-combined image, and smoothed ML-combined image to their corresponding reference image using two

metrics: mean squared error (MSE) and mutual information (MI). Using MI to compare images provides an idea of how well you can predict the signal in one image, given the signal in the first. The more artefact is removed from an image, the more it resembles the image without implant.

Referring to Table 3, we can see that MSE values for the combined images are lower than those of the original images. This confirms that combining the original images using the ML-criterion results in a combined image that is more similar to the reference image, though this is only logical since we are explicitly minimising this difference. Referring to the results Table 4 then, we see that MI values improve as well when using the proposed post-processing technique. For the ML-combined and smoothed ML-combined images, there is an average increase of MI values of 36.13% and 32.58% respectively. Note that this gain is smaller for the SEMAC images. This is because the SEMAC images have already been processed to reduce the size of the artefacts as much as possible. Comparative bar-charts for all four datasets are shown in Figure 21.

Table 3: MSE values for all datasets for the original data, the ML-combined image, and the smoothed ML-combined image.

Dataset	Individual Avg.	Individual Std. Dev	Reconstructed	Reconstructed & Smoothed
Single Carina (MARS)	72.8088e-003	384.9327e-006	65.7573e-003	65.7525e-003
Single Carina (SEMAC)	92.7830e-003	304.3429e-006	87.3866e-003	87.4604e-003
Double Carina (MARS)	9.9288e-003	620.7889e-006	6.1858e-003	5.9846e-003
Double Carina (SEMAC)	8.3754e-003	175.8658e-006	6.8439e-003	6.8452e-003

Table 4: MI values for all datasets for the original data, the ML-combined image, and the smoothed ML-combined image.

Dataset	Individual Avg.	Individual Std. Dev	Reconstructed	Increase	Reconstructed & Smoothed	Increase
Single Carina (MARS)	0.546	0.030	0.771	41.2%	0.744	36.3%
Single Carina (SEMAC)	0.662	0.016	0.867	31%	0.861	30.1%
Double Carina (MARS)	0.708	0.035	1.007	42.2%	0.976	37.9%
Double Carina (SEMAC)	0.804	0.030	1.052	30.1%	1.013	26%

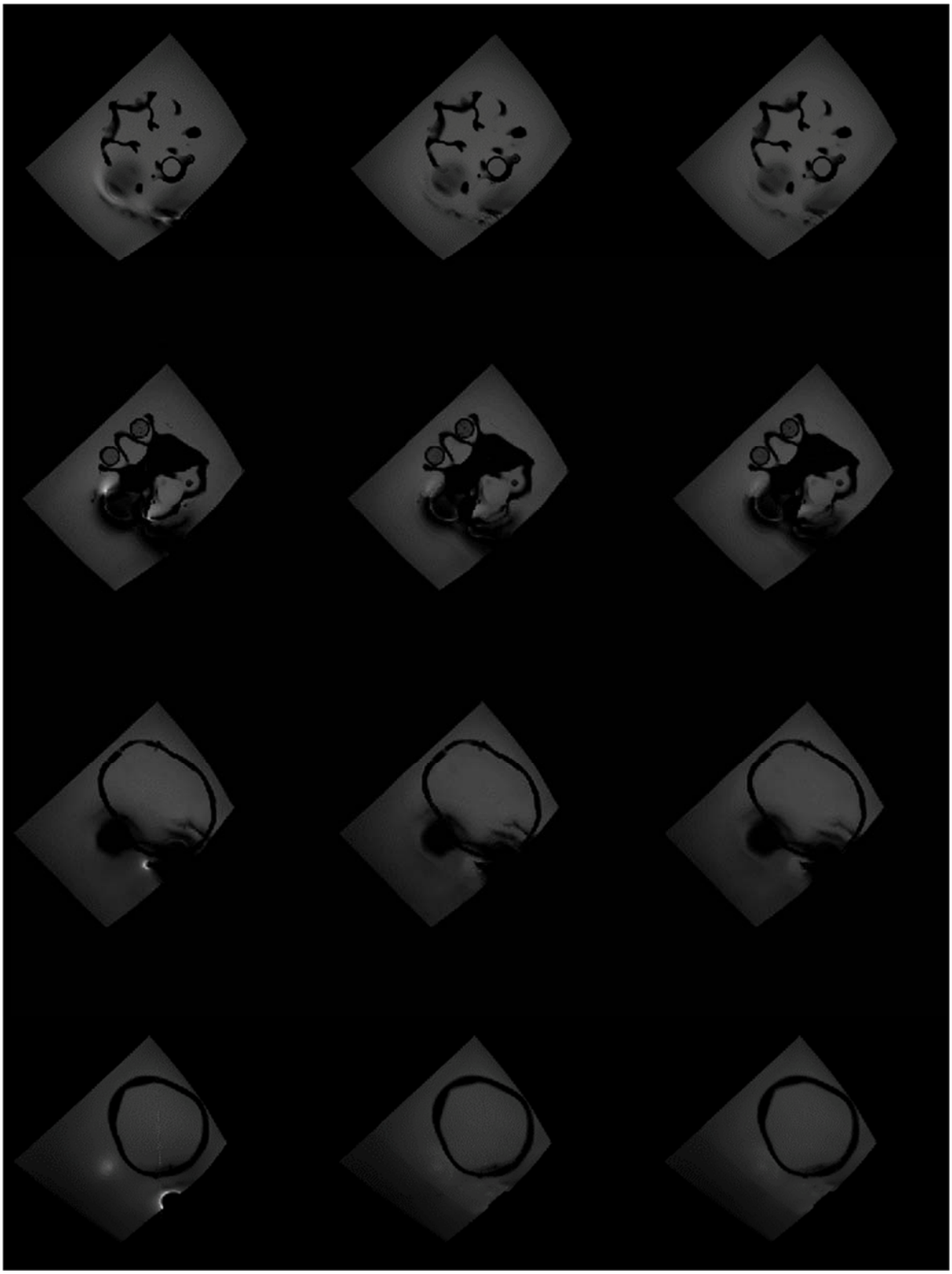

Figure 19: Left to right: arbitrary original scan, ML-combined image, smoothed ML-combined image from CUSTOM sequence.

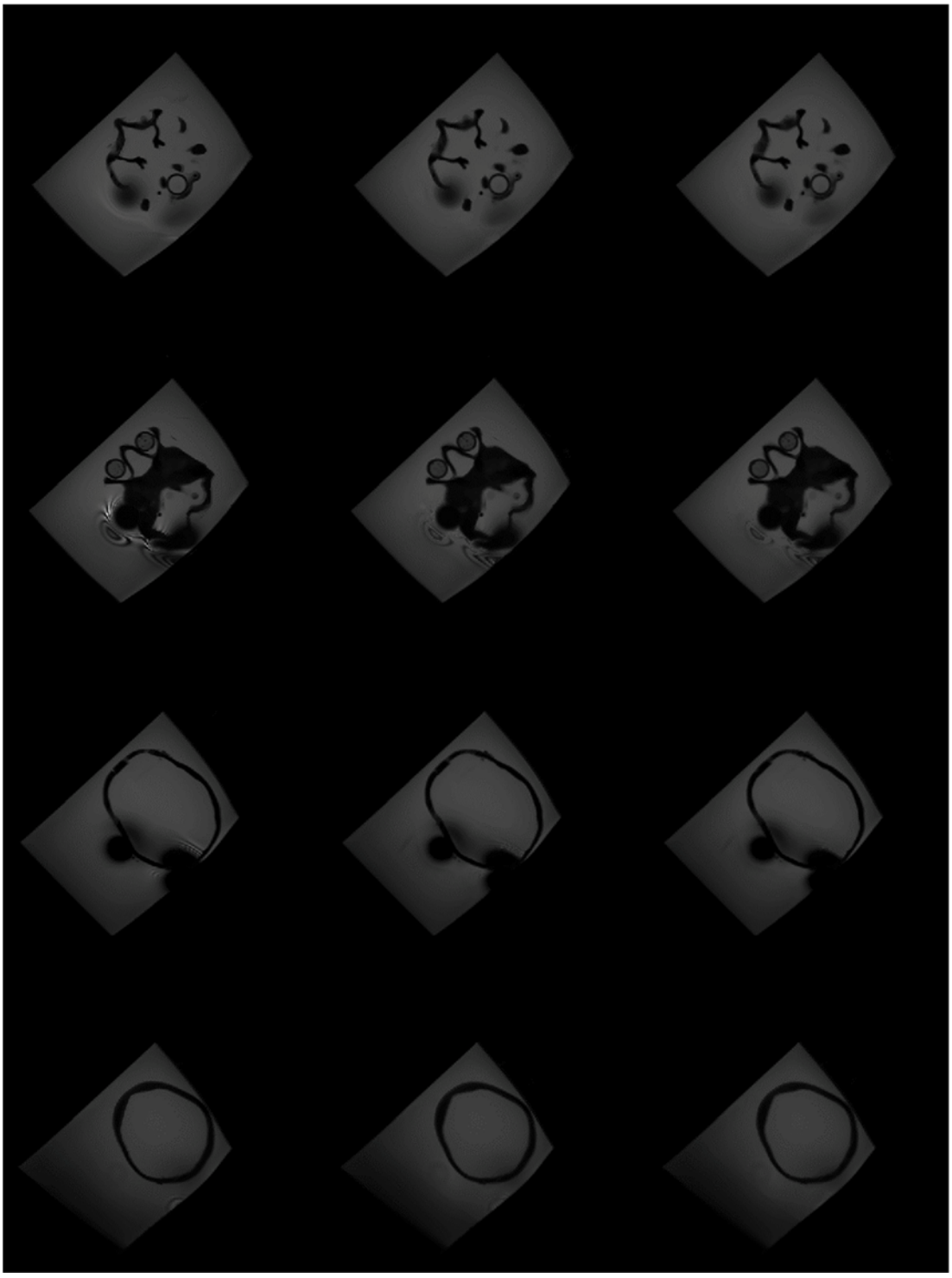

Figure 20: Left to right: arbitrary original scan, ML-combined image, smoothed ML-combined image from SEMAC sequence

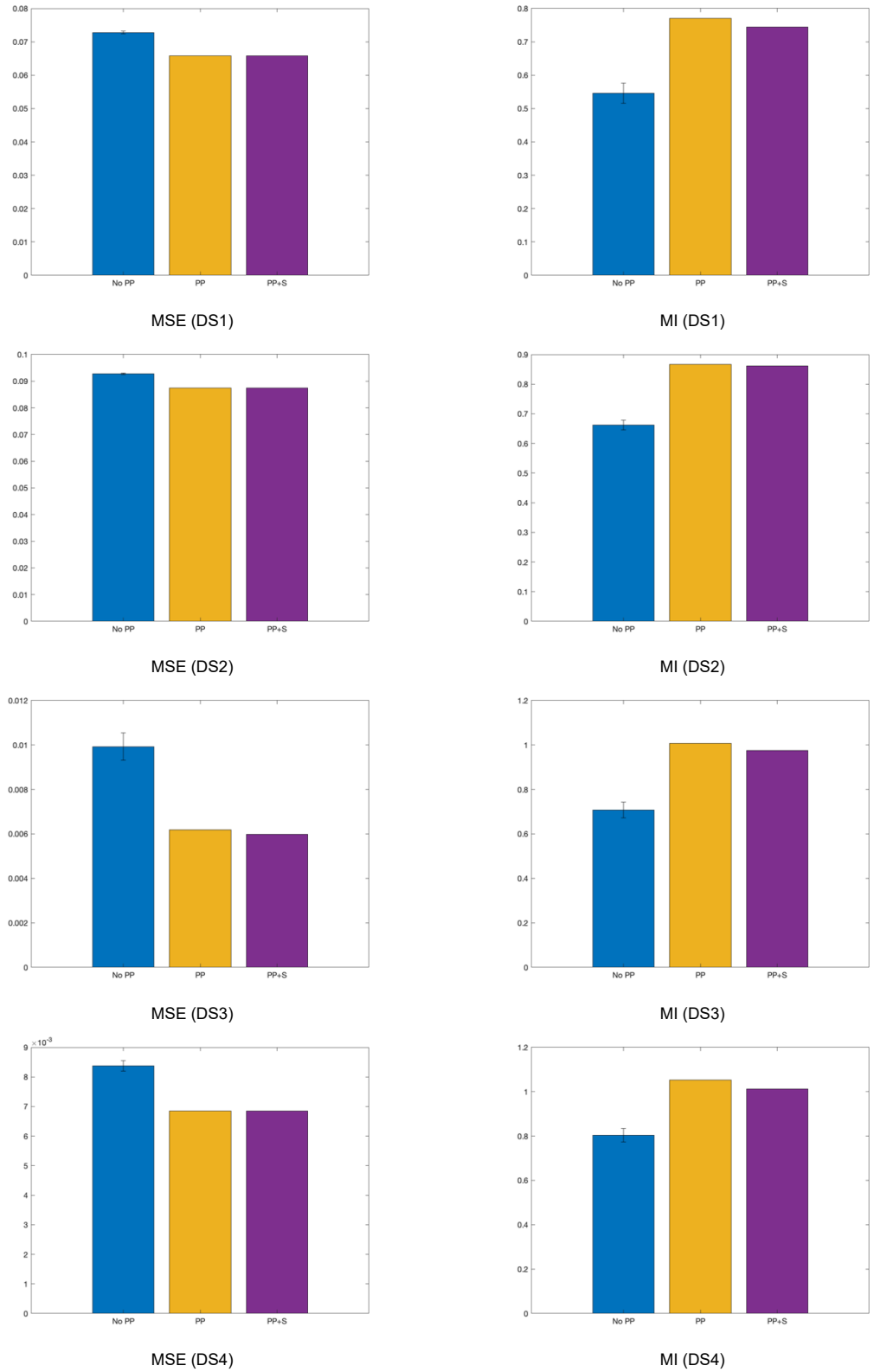

Figure 21: Bar charts for MSE and MI values for all four datasets. In each chart, bars from left to right are from the original images, the ML-combined image, and the smoothed ML-combined image.

6 Conclusions

This document summarised results that were obtained in the scope of deliverable 4.1. Developments from previous WPs were integrated into an active middle ear implant and spinal cord stimulator, which were then tested in single- and multi-implant constellations using various ex-vivo setups. From these experiments, the following conclusion can be made.

First, heating experiments confirmed heating around the SCS, which further increased when a second implant was added. No significant heating was detected around the MEI, though this may have been caused (at least in part) by the positioning of the implant.

Second, artefact sizes for various implant setups were tested. Artefacts around the SCS extended just 1.5cm around the implant, which was significantly less that the artefacts around the MEI. This difference in artefact size is mainly caused by the presence of magnetic materials in the latter. Moreover, we have shown that the size and shape of artefacts is dependent on implant orientation, while no indications were found that artefact geometry changes in cases of multiple implants.

Finally, we proposed a method for reducing artefacts in reconstructed images by combining multiple acquisitions of the same setup with varying frequency and phase encoding directions. Comparing the original and combined images to implant-free reference images using mean-squared error and mutual information metrics, the combined images showed a clear decrease and increase respectively. To the best of our knowledge, this is a first attempt at reducing magnetic susceptibility artefacts in reconstructed images.

7 References

[1] ISO/TS 10974: Assessment of the safety of magnetic resonance imaging for patients with an active implantable medical device (2018)

[2] ASTM Standard F2119, 2007 (2013), “Standard Test Method for Evaluation of MR Image Artifacts from Passive Implants,” ASTM International, West Conshohocken, PA, 2013, DOI: 10.1520/F2119-07, www.astm.org

[3] Fierens, G., Walraevens, J., Paoles, E., Peeters, R., Glorieux, C. (2019). Design of a head phantom for multi-implant image artefact testing in MRI. (Abstract No. 6). Presented at the ISMRM Workshop on MR Safety: Ensuring Safety from First Principles to Best Practices, Utrecht, The Netherlands, 20 Sep 2019-22 Sep 2019.

[4] DISPERSE Consortium, “D2.4 Prototypes for multi-implant assessment, including bench test and EM simulation with typical lead routing”, public deliverable, March 15, 2019.

[5] ASTM Standard F2182, 2011a, “Standard Test Method for Measurement of Radio Frequency Induced Heating On or Near Passive Implants During Magnetic Resonance Imaging,” ASTM International, West Conshohocken, PA, 2013, DOI: 10.1520/F2182-11a, www.astm.org

[6] Hargreaves, Brian A., et al. "Metal-induced artifacts in MRI." American Journal of Roentgenology 197.3 (2011): 547-555.

[7] Huang, Susie Y., et al. "Body MR imaging: artifacts, k-space, and solutions." Radiographics 35.5 (2015): 1439-1460

[8] Metal Artifact Reduction Sequence (MARS) https://radiopaedia.org/articles/metal-artifact-reduction-sequence

[9] Metal Artifact Suppression, http://mriquestions.com/metal-suppression.html

[10] Metal Artefact Reduction, http://www.revisemri.com/blog/2011/metal-artefact-reduction/

[11] Reichert, M., et al. "Metal artefact reduction in MRI at both 1.5 and 3.0 T using slice encoding for metal artefact correction and view angle tilting." The British journal of radiology 88.1048 (2015): 20140601.

[12] S. Klein, M. Staring, K. Murphy, M.A. Viergever, J.P.W. Pluim, "elastix: a toolbox for intensity based medical image registration," IEEE Transactions on Medical Imaging, vol. 29, no. 1, pp. 196 - 205, January 2010. download doi